Precise x-ray energies of gadolinium determined by a combined experimental and theoretical approach

Yves Ménesguen, Marie-Christine Lépy, Y. Ito, M. Yamashita, S. Fukushima, M. Polasik, K. Slabkowska, Ł. Syrocki, E. W der, P. Indelicato, et al.

To cite this version:

Yves Ménesguen, Marie-Christine Lépy, Y. Ito, M. Yamashita, S. Fukushima, et al.. Precise x-ray energies of gadolinium determined by a combined experimental and theoretical approach. Journal of Quantitative Spectroscopy and Radiative Transfer, 2019, 236, pp.106585. 10.1016/j.jqsrt.2019.106585 . hal-03487309

HAL Id: hal-03487309
https://hal.science/hal-03487309v1

Submitted on 20 Dec 2021

Precise x-ray energies of gadolinium determined by a combined experimental and theoretical approach

Y. Ménesguen[1], M.-C. Lépy[1], Y. Ito[2], M. Yamashita[3], S. Fukushima[4], M. Polasik[5], K. Słabkowska[5], Ł. Syrocki[5], E. Węder[5], P. Indelicato[6], J. P. Marques[7,9], J. M. Sampaio[8], M. Guerra[9] F. Parente[9,7], J. P. Santos[9]

[1]CEA, LIST, Laboratoire National Henri Becquerel (LNE-LNHB), bât 602 PC 111, CEA-Saclay, 91191 Gif-sur-Yvette , France

[2]ICR, Kyoto University, Gokasho, Uji, Kyoto 611-0011 Japan[1]

[3]HIT, 3-1-12 Yukihira, Suma-ku, Kobe 654-0037, Japan

[4]Kobe Material Testing Laboratory Co., Ltd., NewSBARU, 1-1-2 Koto, Kamigori, Hyogo 678-1205, Japan

[5]Faculty of Chemistry, Nicolaus Copernicus University in Torun, Gagarina 7, 87-100 Torun, Poland

[6]Laboratoire Kastler Brossel, UPMC-Sorbonne Universités, CNRS, ENS-PSL Research University, Collège de France, Case 74; 4, place Jussieu, F-75005 Paris, France

[7]University of Lisboa, Faculty of Sciences, BioISI - Biosystems & Integrative Sciences Institute, Edificio C8 Campo Grande, 1749-016 Lisboa, Portugal

[8]LIP–Laboratório de Instrumentação e Física Experimental de Partículas, Av. Elias Garcia 14 1D, 1000-149 Lisboa, Portugal

[9]Laboratorio de Instrumentação, Engenharia Biomédica e Fisica de Radiação (LIBPhys-UNL), Departemento de Fisica, Faculdade de Ciências e Technologia da Universidade NOVA de Lisboa, Monte da Caparica, 2892-16 Caparica, Portugal

Abstract

We combined different experimental techniques with a theoretical approach to determine a consistent set of diagram lines energies and binding energies. We propose an original approach consisting in determining the mass attenuation coefficients in an energy range covering the L-, M- and N- absorption edges, including a detailed evaluation of the associated uncertainties, to derive precisely the binding energies. We investigated the $L\alpha$, $L\beta$ and M spectra of Gd with an independantly calibrated high-resolution anti-parallel double-crystal x-ray spectrometer. All the lines were identified and found

---

[1] present adress: Rigaku Corporation, 14-8 Akaoji-cho, Takatsuki, Osaka 569-1146, Japan

in excellent agreement with the binding energies previously derived. Morever, we identified for the first time $M_5 - O_2$, $M_4 - O_{2,3}$ and $M_4 - N_{2,3}$ diagram lines.

1 Introduction

Gadolinium is a lanthanide also known as rare-earth presenting an incompletely filled $4f$ shell, which is responsible for most of the physical properties of the element. The $4f - 3d$ transitions were studied from the theoretical point of view as well as experimentally [1] but the experimental spectra were not deconvolved from the spectrometrist point of view and only the presence of $4f-3d$ and $5p-3d$ transitions was acknowledged. In fact, from the theoretical point of view, the calculation of the $4f - 3d$ transition involves hundreds of thousands of single transitions making it difficult to derive a mean energy or even a relative intensity that fits with the observed spectra. For example when the energy of an elementary transition of a certain diagram line is closer to another diagram line, this leads to a false contribution in an experimental spectrum. Nevertheless, if the experimental resolution of instruments cannot reach the theoretical needs, the analysis of experimental spectra should be deepened in order to deliver a useful and consistent set of energy values for spectrometry issues.

X-ray atomic properties of gadolinium were investigated in a singular approach that combines different experimental techniques to obtain new and useful reliable values of atomic fundamental parameters for x-ray spectrometric purposes. In the litterature, some databases gathered binding energies and/or diagram line energies [2, 3, 4, 5] but they are incomplete or inconsistent. Moreover, associated uncertainties are rarely detailed, which make comparisons more difficult. Therefore, national metrology institutes agreed on the need to improve the reliability of the x-ray fundamental parameters of elements and this work is part of an international effort to aim at this goal [6].

Transition elements and rare-earths, which have incomplete d or f shells present modifications in the atomic spectra due to inter-electronic correlation [7, 8, 9, 10]. For example, the $K\alpha$ and $K\beta$ x-ray emission spectra of the $3d$ transition metals exhibit several peculiar asymmetric line shapes not observed in other elements [11], whose origin has been under investigation and debate [12, 13, 8, 14, 9]. Several mechanisms, such as shake-off and shake-up [15], conduction band collective excitation [16], exchange [17, 18, 19, 20], and final-state interactions [21, 22] were suggested to account for this effect. However, Deutsch *et al.* [8, 14], Hölzer *et al.* [9], Anagnostopoulos *et al.* [23], Chantler *et al.* [24], and Ito *et al.* [25, 26] suggested that the line shapes in $K\alpha_{1,2}$ x-ray spectra could be accounted for by the diagram transition, and $3s$, $3p$, and $3d$ spectator-hole transitions. Ito *et al.* [25] reported that the FWHM of the $K\alpha_{21}$ peak, which includes the satellite lines corresponding to the $K\alpha_2$ line, shows a different aspect from that of the $K\alpha_{11}$ peak, corresponding to a $K\alpha_1$ line, which may be ascribed to the $L_2 - L_3M_{4,5}$ Coster-Kronig transitions. Moreover, Ito *et al.* [26] measured systematically the $K\alpha_{1,2}$ spectra of the elements from Ca to Ge using an antiparallel two-crystal x-ray spectrometer. Combined with *ab initio* Dirac-Fock calculations, the origin of the asymmetry in the $K\alpha_{1,2}$ spectra for Ca, Ti, and Ge elements can be fully explained by considering only the diagram and the $3d$ spectator transitions, such as shake-processes.

The $K\beta_{1,3}$ x-ray emission spectra includes $K\beta'$ and $K\beta''$ satellites on the low- and high-energy side of the $K\beta_{1,3}$ peak position, respectively, as explained in the case of copper [8, 14]. These satellites have also been investigated until now both experimentally and/or theoretically [11, 9, 23, 27, 28, 29, 30, 31, 32] for all $3d$ transition metals. Shake-up from the $3d$ shell was also shown to account reasonably well for the measured $K\beta_{1,3}$ line shape, although a complete quantitative fitting has not been reported and possible contributions from other shells were not investigated [27, 30]. The low-energy satellite group, denoted by $K\beta'$, received special attention, and several other sources such as exchange interaction [17, 18, 19, 20] and plasmon oscillations [21, 22] were suggested to be their origin. It has been assumed that the line shape can be fully accounted for by satellites resulting from $3l(l = s, p, d)$ spectator holes in addition to the nominal single-electron diagram transitions. Recently, The $K\beta$ x-ray spectra of the $3d$ transition metals from Ca to Ge have been systematically investigated either experimentally, using a high-resolution antiparallel double-crystal x-ray spectrometer, and theoretically [33]. Each $K\beta_{1,3}$

natural line width has been corrected using the instrumental function of this type of x-ray spectrometer, and the spin doublet energies have been obtained from the peak position values in $K\beta_{1,3}$ x-ray spectra. For all studied elements, the corrected $K\beta_1$ x-ray lines FWHM increase linearly as a function of Z. However, for $K\beta_3$ x-ray lines this dependence is generally not linear in the case of $3d$ elements but increases from Sc to Ni. Moreover, the theoretically predicted synthetic spectra of Ca, Mn, Cu, and Zn are in very good agreement with the observed data except for the case of Mn, due to the influence of the complicated structure of the metallic Mn. They suggested that the contributions of satellite lines in $3d$ $K\beta_{1,3}$ spectra are considered to be $[KM]$ shake processes similar with that in $3d$ $K\alpha_{1,2}$ spectra.

On the other hand, and to our knowledge, there were not carried on the studies considering the instrumental function for the L and M emission lines of the lanthanides as it has be done for $K\alpha$ and $K\beta$ lines in $3d$ elements. Regarding the L x-ray emission spectra for the lanthanide compounds, the studies have been focussed mainly on the chemical shifts, intensity ratios, and their line shapes [34, 35, 10, 36]. This work present for the first time detailed measurements of $L\alpha$ and $L\beta$ diagram lines on metallic Gd considering the instrumental function to derive the natural linewidths. Concerning the M spectral lines, several experimental works were performed using XPS or XES in some lanthanide compounds together with theoretical works [37, 38, 39, 40, 41, 42, 1, 43, 44] or in metallic and oxide of Gd [45, 46, 47] in order to identify the main components. In this work, we combine several experimental approaches as well as new theoretical calculations to derive a consistent set of atomic binding energies of metallic gadolinium. We present accurate measurement of mass attenuation coefficients in the range 100 eV to 25 keV that are used to derive the binding energies. This allowed to identify some x-ray diagram lines present as weak lines on the high-resolution spectra obtained by the double-crystal x-ray spectrometer and the electron-probe micro analyser (EPMA). The energy positions of the diagram lines are determined experimentally and compared with our theoretical values and found in excellent agreement.

2 The Mass attenuation coefficients and absorption edges

2.1 Experimental determination of the mass attenuation coefficients

The methodology used to determine the mass attenuation coefficients was extensively described in [48, 49, 50] and consequently, will not be detailed here. The mass attenuation coefficient, ${}^{\mu}/_{\rho}$, is the parameter standing for the interaction probability of a photon beam with matter. It depends both on the material and the photon energy and includes the photo-absorption and scattering effects. The overall attenuation of a parallel and monochromatic photon beam at normal incidence through a thin target follows the Beer-Lambert law, from which the mass attenuation coefficients can be derived,

$$ {}^{\mu}/_{\rho} = \frac{-1}{\rho \times x} \times \ln\left(\frac{I}{I_0}\right) = \frac{-A}{M} \times \ln(T) \tag{1} $$

where I and I_0 are the transmitted and incident photon beam intensities, respectively, ρ and x are respectively the target density and thickness, μ/ρ is the energy-dependent mass attenuation coefficient, M is the mass of the target, A its area, and T is the transmission ratio. The procedure using a monochromatic photon beam of low divergence is a convenient way to determine this parameter. In this approach, the final uncertainty budget is linked to the target characteristics and the photon flux intensities.

The experimental transmission measurements were done in an energy range covering the L, M and N_{1-5} absorption edges using the two branches of the SOLEIL metrology beamline, the hard x-ray branch from 3 to 25 keV, the xuv branch from 100 to 1.8 keV, and the laboratory source SOLEX for energies between 1.8 to 3 keV.

At the SOLEIL synchrotron (France), the metrology beamline optics were aligned as described in [48] to minimize harmonics and stray light, and the Bragg angle was calibrated with respect to K-absorption edges of pure metal foils. The Bragg angular position is equipped with an optical encoder and only one calibration point is needed. If different elements were used in [48], only a maximum residual discrepancy of 0.04% between the tabulated K-absorption edge and the measured one over the whole energy range when calibrating the Bragg angle with one edge only. Therefore, the K-absorption edge of zirconium was chosen for calibration of the Bragg angle of the two-crystal Si(111) monochromator (hard x-ray branch) and aluminum K-absorption edge for the grating at low energies (xuv branch), respectively. The transmission measurements were performed using a beam collimated at 2.5 × 2.5 mm^2 at normal incidence, thus considering the area representative of the average thickness of the whole target. Once the energy calibration is achieved, long scanning sequences with 50 eV steps are carried out within the entire available photon energy range, with smaller steps of 3 eV around the L-absorption edges and 1 eV around the M- and N-absorption edges. The transmitted photon intensities are recorded by means of an AXUV:Al photodiode whose dark noise is subtracted from acquired current values to derive an unbiased transmittance.

The laboratory x-ray source SOLEX was also used to cover the energy gap between the hard x-ray and xuv branches using the Si(111) and Béryl($10\bar{1}0$) crystals as monochromators [51]. The weak flux delivered by this source, compared to a synchrotron beamline, constrained us to use an energy-dispersive spectrometer as detector, which has the advantage of simply discriminating stray light and harmonics at the expense of a higher statistical uncertainty.

Accurate values of the sample characteristics are required to derive absolute values of the mass attenuation coefficients. Gadolinium was studied in the form of metal foils, supplied by the Goodfellow corporation [52], which were chosen with a mass purity better than 99.9 %. To derive absolute mass attenuation coefficients from Equation (1), mass per unit area must be known with the lowest possible uncertainty. The samples were weighed with a calibrated microbalance used in a laboratory whose ambient air hygrometry, temperature and pressure are controlled giving an absolute uncertainty of 9 µg at best. The area was measured with a Mitutoyo QSL-2010Z vision machine consisting of a microscope with two calibrated stages and a picture analyzer. Three samples were used in the different SOLEIL transmission experiments. The thickest of nominal thickness 10 µm was weighted 10.664(10) mg with an area of 135.52(10) mm^2. The 2 µm foil weights 1.575(9) mg with an area of 102.43(10) mm^2. Measuring the mass and area of the samples has the advantage to be more accurate and independent from x-ray analysis techniques, nevertheless, the thinnest foil of nominal thickness 0.2 µm could not be handled and its mass per unit area was determined at 2.48 × 10^{-4}g.cm^{-2} by scaling the experimental results of the transmission measurements for the product of mass attenuation coefficient, and mass per unit area to the hard x-ray data in overlapping energy ranges.

2.2 Results and uncertainty estimation

Equation (1) can be modified by including a factor $k_P = 1$, which is responsible for an additional uncertainty due to the elemental purity, calculated as in [48]:

$$\mu/\rho = \frac{-A}{M} \times \ln(T) \times k_P \tag{2}$$

N°	Sample 10 µm (%)	Sample 2 (%)	Sample 0.2 µm (%)
Mass	0.097	0.6	-
Area	0.08	0.1	-
Mass/Area	-	-	1
Sample purity	0.5	0.5	0.5
Transmission	0.17	1.8	0.16

Table 1: Uncertainty budget: relative standard uncertainties of each contributor.

To evaluate the uncertainty of the experimental mass attenuation coefficients, Eq. (2) was derived according to all the influence quantities, as mentioned in the “Guide to the expression of uncertainty in

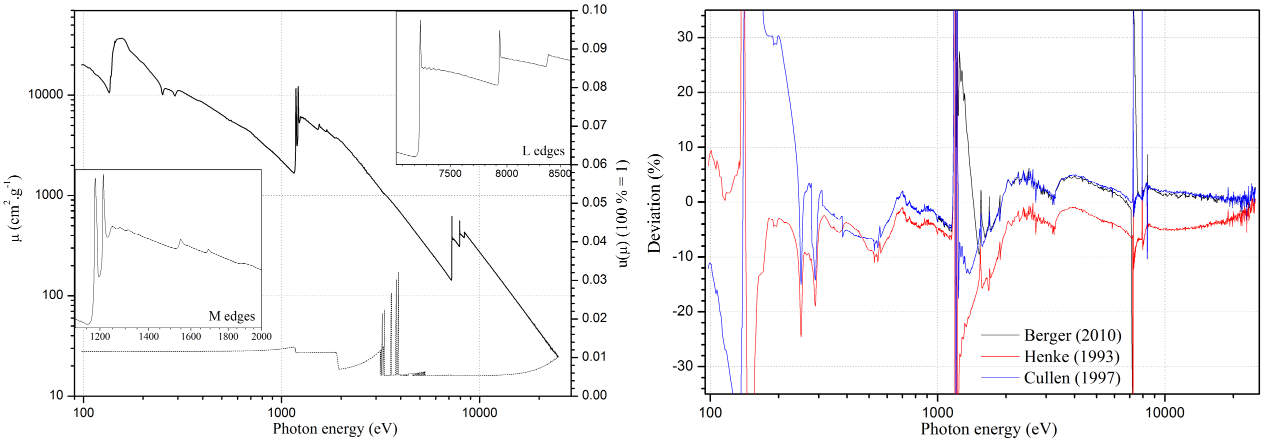

Figure 1: Left: Mass attenuation coefficients of Gd (as metal) measured from the N to the L absorption edges (values on the left-hand vertical axis). The lower data points represent the relative standard uncertainties (right-hand vertical axis, where 0.10 means 10 %). The inset graphs are details of the mass attenuation coefficients of Gd around the L and M-absorption edges. Right: Comparison of experimental values with published databases; the relative deviation as calculated by Eq. (4) is plotted for the databases referenced therein.

measurement" [53]. The combined standard uncertainty is, thus expressed using the following formula:

$$\left(\frac{u(\mu/\rho)}{\mu/\rho}\right)^2 = \left(\frac{u(M)}{M}\right)^2 + \left(\frac{u(A)}{A}\right)^2 + \frac{\left(\frac{u(T)}{T}\right)^2}{\ln(T)^2} + \left(\frac{u(k_P)}{k_P}\right)^2 \qquad (3)$$

where the relative uncertainty of the transmission is estimated in the same way as in [48]. Table 1 gives the different contributions to the uncertainty budget of the mass attenuation coefficient measurements. For the mass attenuation coefficients in the soft x-ray range, the different contributions cannot be written in the form of Eq. (3) because mass and area were not measured. Instead, the contributions to the uncertainty budget were obtained from the matching of the different data sets (1.0 %).

The measurements resulted in a set of transmission data for metallic Gd in the photon energy range from 0.1 keV to 25 keV, from which the energy dependent mass attenuation coefficient was calculated, covering the M-, L- and some N-absorption edges (Fig. 1).

These results were compared to theoretical and experimental values compiled in other published studies or databases such as [54, 55, 4, 56]. The relative differences between the present results and other tabulated values are presented in Fig. 1 right. This graph plots the relative deviation as stated in Equation 4:

$$\frac{\Delta\mu}{\mu} = \frac{\mu_{EXP} - \mu_{DB}}{\mu_{DB}} \times 100 \qquad (4)$$

where μ_{EXP} denotes for the presently measured mass attenuation coefficients and μ_{DB} stands for values from a published database. The largest relative difference found around the M- and L- absorption edges are essentially due to the fine structures which are detailed in the present measurements. The $\Delta\mu/\mu$ deviation plotted for the data from Cullen [4] and Berger [56] can be as high as 3% for photon energies larger than the Gd L_1 absorption edges and even higher deviations with the Henke data [54] are observed. At higher photon energies, the behaviour of Henke's values differs from the others of where no significant deviations were found. It must be noted that all the uncertainties reported by Krause et al. [57] are very high and not even known for energies below the L absorption edges of any element.

2.3 L-, M- and N- absorption edges

The mass attenuation coefficients were measured on a large energy range including the L and M-absorption edges. The energy scale was calibrated using the experimental values of the Deslattes database [5]. The K-absorption edges are presumably the most reliable and only a residual difference of 0.04% was measured [48] for several K-absorption edges (Ti, Fe, Cu, Zr, Mo, Rh, Ag). The Deslattes Zr K-absorption edge is 17995.87(8) eV, and it is proposed to be 17997.6 eV by Larkins [2], and 17995.2 eV by Cauchois [3], that is to say a relative difference of 0.01 % and 0.004 %, respectively.

We estimated the L and M absorption edges of gadolinium at the inflexion point of the mass attenuation coefficients curve. It was estimated by taking the position of the maximum of a fitted gaussian curve on the first derivative of the mass attenuation coefficients, except for $L_{2,3}$ and $M_{4,5}$ because a strong peak, due to bound states interactions, is red-shifting the edge. Instead, we modelled the absorption edge by a gaussian curve representing the bound states superimposed with a step function representing the edge. The inflexion point of the step function is used to derive the value of the absorption edge. The results are presented in Table 2. The best agreement of our values is observed with the database from Larkins [2] concerning the L and $M_{1,2,3}$-absorption edges. On the other hand, we found a better agreement with values from Cauchois [3] for the $M_{4,5}$-absorption edges.

Edge	This work	Deslattes [5]	Cauchois [3]	Larkins [2]	Cullen [4]
L_1	8377.3(10)	8381.7(14)	8386.2	8375.6	8349.8
L_2	7930.0(30)	7934.3(11)	7931.0	7930.3	7947.0
L_3	7246.6(28)	7246.6(9)	7242.9	7242.8	7242.7
M_1	1884.0(10)	*1884.61*		1880.8	1864.6
M_2	1686.9(5)	*1694.4*		1688.3	1686.9
M_3	1543.5(5)	*1550.7*	1542.9	1544.0	1541.8
M_4	1220.1(6)	*1221.61*	1213.1	1217.2	1231.6
M_5	1190.1(27)	*1189.23*	1183.9	1185.2	1199.8
N_1	383.0(10)			375.8	381.39
N_2	292.0(10)			288.5	311.3
N_3	253(10)			270.9	278.86
N_4	143.0(10)		149.4	140.5	162.16
N_5	139.0(10)			140.5	156.16
$N_{6,7}$	*11.3(12)*			0.1	16.2
O_1				36.1	34.83
O_2	*30.7(10)*			20.3	30.18
O_3	*25.5(10)*			20.3	17.03

Table 2: Experimental binding energies derived from the absorption edges of gadolinium (in eV). In the present work, the values in italic are derived from the M lines. In the Deslattes column, italic values are derived from the difference between the L experimental absorption edges and diagram lines quoted in [5].

3 Theoretical models for the diagram lines

Theoretical predictions of the Gd L and M x-ray diagram line positions have been performed using the multiconfiguration Dirac-Fock (MCDF) method, which is the primary theoretical tool applied in atomic physics, allowing for the determination of many of the significant atomic parameters. The MCDF method is described in detail in many papers [58, 59, 60, 61, 62, 63, 64, 65, 66, 67, 68, 69, 70]. Thanks to the ease of performing high-precision large-scale calculations, it is even possible to include electron correlations to a large extent. Our calculations have been done with the GRASP (General-Purpose

Relativistic Atomic Structure Package) package [59, 66, 67], and with the Relativistic General Purpose Multiconfiguration Dirac-Fock code (MCDFGME) developed by Desclaux and Indelicato [69, 70]. The effective relativistic Hamiltonian for an N-electron atom is given by (Eq. 5)

$$\widehat{H}=\sum_{i=1}^{N}\hat{h}_D\left(i\right)+\sum_{j>i=1}^{N}V_B\left(i,j\right) \tag{5}$$

where $\hat{h}_D\left(i\right)$ is one-electron Dirac Hamiltonian, and $V_B\left(i,j\right)$ describes the sum of Coulomb interaction and Breit interaction between the i-th and the j-th electron. The wave function describing an N-electron atomic state, characterized by the total angular momentum J, the projection value of angular momentum M, and parity p, is assumed in the form [58], (Eq. 6)

$$\Psi_S\left(JM^p\right)=\sum_{m}c_m\left(s\right)\Phi\left(\gamma_m JM^p\right) \tag{6}$$

where $\Phi\left(\gamma_m JM^p\right)$ are N-electron configuration state functions (CSFs) built from one-electron Dirac spinors, $c_m\left(s\right)$ are the configuration mixing coefficients for state s, and γ_m contains all information necessary to uniquely define the respective CSFs. All the states (with given quantum numbers) corresponding to the set of initial and final configurations are simultaneously taken into account in the MCDF calculations [60, 61, 62, 63, 64, 65] to determine the x-ray line positions and spectra structure. It must be underlined that the application of the relativistic MCDF method, taking into account Breit interaction and two quantum electrodynamics (QED) corrections (self-energy and vacuum polarization), and a finite size nucleus model (with a two-parameter Fermi charge distribution) is crucial to reliably determine the significant atomic parameters with the highest possible accuracy. We expect the accuracy of the simulations to be high, partly because some of the approximations included in the code tend to affect the energy values involved in a similar way, so that their effect may partly disappear from differences. Consequently, we estimate that the associated uncertainty for the calculated positions of the lines is 0.2 eV at worst.

The theoretical values are presented in Tables 5 and 6 together with the experimental values and Bearden's and Deslattes experimental ones.

4 X-ray emission spectroscopy

4.1 Experimental determination of L diagram lines

In the present work, we used a Rigaku (3580EKI) double-crystal spectrometer integrated in a chamber of which the temperature is controlled within 035.0 ± 0.5°C. The experimental conditions for the measurements are given in Table 3, and a metal foil sample of gadolinium (Nilaco Co. Ltd., purity of 99.9 % with an impurity of ~0.1 % of Fe) was used. Using this spectrometer, the true full-width at half-maximum (FWHM) of the emission line can be determined by a simple subtraction of the convolution in the crystal dispersion from the FWHM of the measured emission line [26, 33] (see Ref. [71] for details). With a Rh end-window x-ray generator operated at 40 kV, 60 mA, the emitted L spectra in Gd (see Figs.2, 3, and 4) were recorded with a gas proportional counter in the symmetric Si (220) and Ge(220) Bragg reflection of the double-crystal spectrometer at an angular step of 0.001 or 0.002 degree in 2θ. The vertical divergence slit is 0.573 degree in this spectrometer. Acquisition time was 20 to 80 s/point (see Table 3). We checked the Cu $K\alpha_{1,2}$ diagram lines as standard lines in order to evaluate the reproducibility in the double-crystal x-ray spectrometer while measuring the Gd $L\alpha_{1,2}$ and $L\beta_{1,4}$ diagram lines for comparison with those reported by Ito et al. [26]. An example of these results is presented in Table 4 for the Cu $K\alpha_{1,2}$ lines. The CF values of the $K\alpha_{11}$ and $K\alpha_{21}$ diagram lines are very consistent with those of the lines from Ito et al. [26] (Table 4). Neither smoothing nor correction was applied to the raw data. Each spectrum was repeated three times. The values of Deslattes' et al. [5] were used as initial parameters for the L diagram lines in the fitting process.

line	analyzing crystal	accumulation time (s/point)	step (deg.2θ)	Voltage (kV)
$L\alpha_{1,2}$	Si(220)	60	0.001	40
$L\beta_{1,4}$	Si(220)	80	0.001	40
$L\beta_{1,2,3,4,6,9,10,15}$	Ge(220)	20	0.002	40

Table 3: Experimental conditions of the measurements using a two-crystal x-ray spectrometer on a metallic foil of gadolinium . The measurements were repeated 3 times under vacuum with a rhodium anode at 60 mA current.

Lines	Energy (eV)	FWHM (eV)		AI	NIR
		Exp.	Campbell [72]		
$K\alpha_1$	8047.76(8)	2.696(9)		1.155(7)	100
$K\alpha_2$	8027.73(8)	3.134(24)		1.150(12)	50.92(20)
$\Delta E_0(K\alpha_1 - K\alpha_2)$	20.03(4)				
$K\alpha_{11}$	8047.76(8)	2.243(14)*	2.1		100
$K\alpha_{12}$	8045.23(9)	2.99(13)			10.99(69)
$K\alpha_{21}$	8027.96(5)	2.56(5)*	2.53		40.6(21)
$K\alpha_{22}$	8026.38(7)	3.22(10)			16.5(22)
$\Delta E_0(K\alpha_{11} - K\alpha_{21})$	19.79(4)				

Table 4: The averaged fitting parameters for the Cu $K\alpha_{1,2}$ spectra using four symmetric and two asymmetric Lorentzians. A four Lorentzian functions fitting is used for the contribution of the shake processes and obtaining the natural linewidths. NIR stands for the normalized intensity ratio, AI stands for asymmetric index, * is the CF, i.e. the corrected FWHM from the instrumental resolution. In order to investigate the stability of the spectrometer, Cu $K\alpha_{1,2}$ emission lines were measured as the standard lines. The primary target was Rh and the spectrometer crystal was Si(220) x 2.

4.1.1 The observed $L\alpha$, $L\eta$ and $L\beta$ emission spectra of gadolinium

The Gd $L\alpha_{1,2}$ and $L\eta$, and $L\beta_{1,2,3,4,6,9,10,15}$ spectra were measured several times using a high-resolution double-crystal x-ray spectrometer. These emission spectra are shown in Figs. 2, 3 and 4, respectively. We measured the Gd $L\alpha, \beta$ spectra with Cu $K\alpha_{1,2}$ standard spectra in order to check the reproducibility of the double-crystal spectrometer. Thus, the measurement sequence is repeated three times as follows; Cu $K\alpha_{1,2}$-Gd L lines-Cu $K\alpha_{1,2}$-Gd L lines-Cu $K\alpha_{1,2}$-Gd L lines-Cu $K\alpha_{1,2}$ (Table 4). Actually, to obtain realistic uncertainties, the ones originating from the energy calibration have to be considered. For example, absolute $K\alpha_{1,2}$ and $K\beta_{1,3}$ photon energies for all $3d$ elements from Cr to Cu can be found in [9]. A well-known identification of the line shape is generally based on its FWHM and its intensity ratio in x-ray emission lines. Both values allow for a comparison with other experimental results and a general classification of our measurements relative to other reference data. However, it is noteworthy that various width values from previous measurements on the elements do not include complete corrections for the instrumental broadening [9, 26]. The advantage of the double-crystal spectrometer setup lies in the fact that the true FWHM of the emission line can be determined by a simple subtraction of the crystal dispersion from the FWHM of the measured emission line [71]. This approach was employed in this work. The averaged line energies, observed FWHM, corrected FWHM (CF), and relative intensity ratio in each Lorentzian model were determined as shown in Tables 5, 6 and 7, together with the recommended natural line widths [72]. The Lorentzian fitting model was used for an analytical representation of these lines [8, 9, 26, 33]. The uncertainties quoted in Tables 5, 6 and 7 are thus only statistical uncertainties resulting from the fitting processes, and the limited reproducibility of the experimental setup.

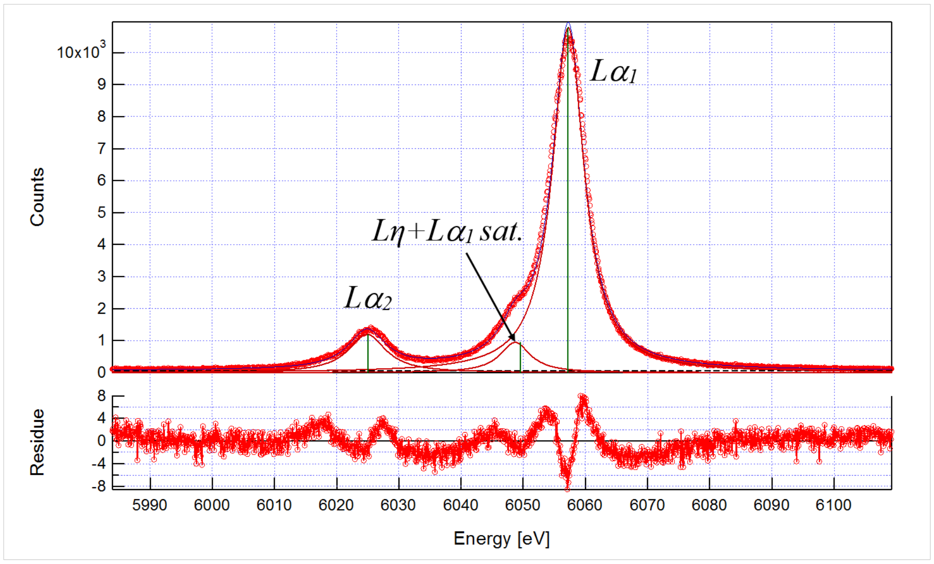

Figure 2: The observed $L\alpha_{1,2}$ spectra of gadolinium shown with the Lorentzian functions used in the fitting process [8, 73, 26, 33] were measured using the antiparallel double-crystal x-ray spectrometer with Si(220) crystals.

Lines	Energy (eV)					FWHM (eV)		NIR
	Present		Cauchois	Deslattes [5]		CF	Campbell	
	Exp.	Th.	[3]	Exp.	Th.	Exp.	[72]	
$L\alpha_1$ $(L_3 - M_5)$	6056.85(34)	6057.50(20)	6057.24	6057.37(88)	6057.8(11)	6.159(23)	4.67	100
$L\alpha_2$ $(L_3 - M_4)$	6024.51(33)	6023.00(20)	6025.03	6024.99(87)	6024.0(12)	7.28(7)	4.67	13.04(16)
$L\eta$ $(L_2 - M_1)$*	6048.36(30)	6047.91(20)	6049.27	6049.69(44)	6048.3(16)	5.89(16)	16.67	8.40(32)

Table 5: The averaged fitting parameters for the Gd $L\alpha_{1,2}$ spectra using three symmetric Lorentzians, deriving the natural linewidths. NIR stands for the normalized intensity ratio, CF are the corrected FWHM from the instrumental resolution. * indicates that the $L\eta$ diagram line superimposes the $L\alpha_1$ satellite. The energy values are from Cauchois [3] and Deslattes *et al.* [5], respectively, and the FWHM are from Campbell and Papp [72]. Uncertainties are indicated within parentheses. The primary target was Rh and the spectrometer crystal was Si(220) × 2.

4.1.2 $L\alpha_{1,2}$ and $L\eta$ emission spectra

In Table 5 we present the averaged energy, FWHM, CF and intensity ratios of the $L\alpha_1$, $L\eta$, and $L\alpha_2$ diagram lines together with the recommended FWHM reported by Campbell and Papp [72] for Gd. We obtained the CF values for the $L\alpha_{1,2}$ and $L\eta$ diagram lines from the observed FWHM through Tochio's method [71]. As mentioned in Table 5, the CF values of these $L\alpha_{1,2}$ $(L_3 - M_{4,5})$ lines are larger than those from Campbell and Papp [72]. However, that of $L\eta$ $(L_2 - M_1)$ line, 5.850 eV, is much smaller than the one quoted in [72], i.e. 16.67 eV. The physical meaning of this difference in the $L\eta$ diagram line is not clear. Moreover, the energy values of $L\alpha_{1,2}$ and $L\eta$ lines are calculated and presented in Table 5. They are very consistent with the observed ones as seen in this table.

Krish *et al.* [74] performed experiments on the evolution of the $L\alpha_1$ spectral line profile for energies larger than the L_3 edge and below the L_2 absorption edge. They also performed resonant-Raman scattering experiments in the vicinity of the L_3 absorption edge [75] to study the multi-electron transitions such as shake processes. Our $L\alpha_{1,2}$ spectral profiles are very similar with those of Krish *et al.*, consequently, we could not be able to distinguish the $L\eta$ diagram line from $L\alpha_1$ satellite as they

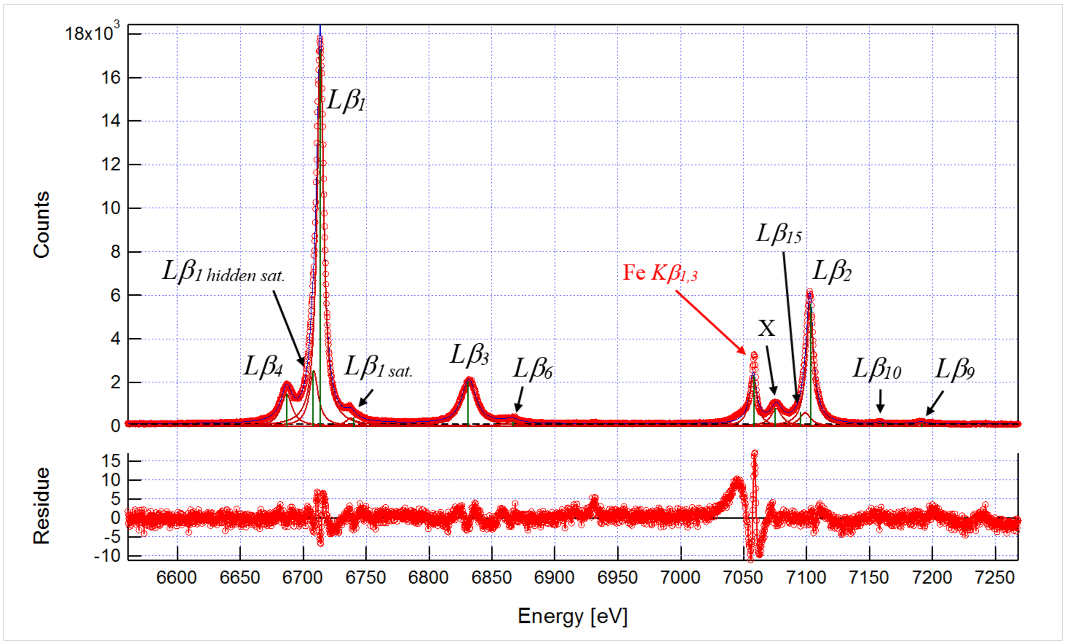

Figure 3: The observed $L\beta_{1,2,3,4,6,9,10,15}$ spectra of gadolinium shown with the Lorentzian functions used in the fitting process [8, 73, 26, 33] were measured using the antiparallel double-crystal x-ray spectrometer with Ge(220) crystals.

superimpose.

4.1.3 $L\beta$ emission spectra

For the measurements of these spectra, we used a Ge(220) double-crystal monochromator in the x-ray spectrometer in order to investigate the intensity ratio of each diagram line more accurately. The observed spectra of $L\beta_{1,2,3,4,6,9,10,15}$ emission lines are shown in Fig. 3. In Table 6, the diagram lines, the averaged energy, FWHM, and intensity ratio are shown together with the recommended values reported by Campbell and Papp [72], the experimental ones reported by Cauchois [3] and Deslattes et al. [5], and theoretical values [5], respectively. The photon energy, FWHM, and the intensity ratio in each diagram line were obtained using the fitting analyses. The $L\beta_1$ diagram line has a hidden satellite. In order to make the reconfirmation of this satellite, the regions of the $L\beta_1$ and $L\beta_4$ spectral lines were measured using the Si(220) analyzing crystals (Fig. 4). The averaged FWHM or corrected FWHM (CF) and intensity ratio of $L\beta_1$, $L\beta_4$, $L\beta_1$ visible satellite and $L\beta_1$ hidden satellite lines are presented in Table 7 together with the recommended FWHM [72]. The CF of $L\beta_1$ diagram line is larger than the recommended one, that is, 5.87(4) and 4.82 eV, respectively. Moreover, $L\beta_{15}$ line was confirmed at the photon energy of 7098.2(7) eV and is in excellent agreement with the value 7097.92 eV reported by Cauchois [3].

The peak at 7075 eV marked by X corresponds to the $L\beta_{14}$, an $L\beta_2$ satellite line reported by in the table from Cauchois [3], originally in [77]. Krish et al. [74] observed the line "X" on such a spectrum on the low energy side of the $L\beta_{2,15}$ diagram lines, using an excitation energy higher than the L_3 absorption edge and lower than the L_2 edge. According to their suggestions, the two main peaks in the $L\beta_{2,15}$ emission spectrum are not due to the spin-orbit interaction in the $4d$ shell, which is less than 0.2 eV. They are rather caused by magnetic and electrostatic interactions between the $4d$ and $4f$ electrons. The two lines, separated by ~ 27 eV in their case and 26.42 eV in our case, are due to configurations with the spin of $4d$ electrons either mostly parallel (line at 7102.104 eV) or antiparallel (line at 7075.692 eV) to the spin of the $4f$ electrons. The ejected photoelectron has dominantly spin-up character for the

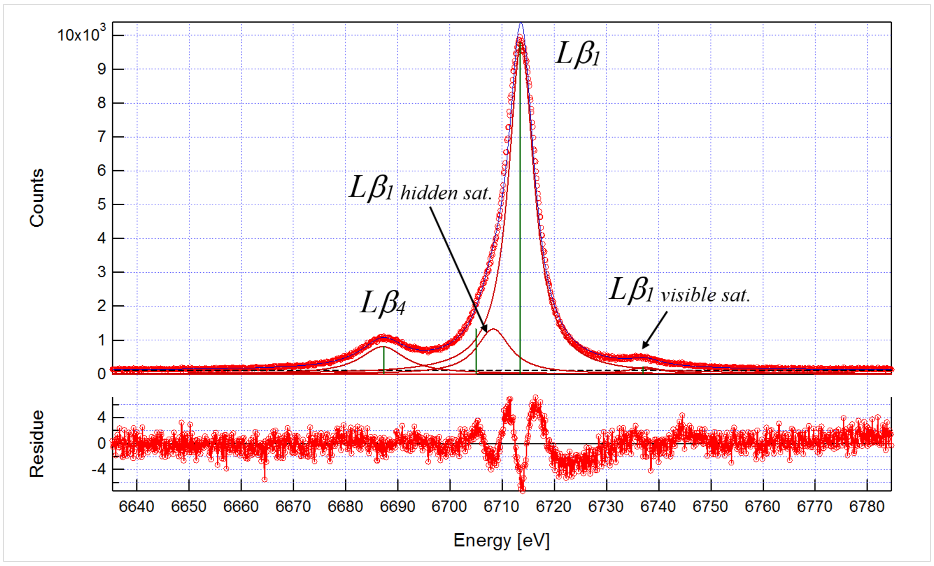

Figure 4: The observed $L\beta_{1,4}$ spectra in gadolinium are shown with Lorentzian functions used in the fitting process [8, 73, 26, 33]. These spectra were measured in details using the antiparallel double-crystal x-ray spectrometer with Si(220) crystals described in the text. The $L\beta_1$ visible satellite was identified and the $L\beta_1$ hidden satellite was newly found.

line at 7075.69 eV and spin-down character for the line at 7102.10 eV.

4.2 Experimental determination of M diagram lines

We have investigated Gd $M\xi$, $M\alpha$, $M\beta$ and $M\gamma$ emission lines in detail using both the photon and the electron bombardment methods. The former analyser is the anti-parallel x-ray spectrometer and the latter is EPMA, respectively, and both spectrometers are using TAP(001) double-crystals. In the photon bombardment method, the rhodium end-window generator was operated at 30 kV, 60 mA. The emitted $M\alpha, \beta, \gamma$ spectra of Gd were recorded with a gas proportional counter accumulating 20 seconds per point, in the symmetric TAP(001) Bragg reflection of the double-crystal spectrometer at an angular step of 0.005 degree in 2θ. The values of Bearden's et al. [76] were used as initial parameters for the M diagram lines in the fitting process. In the electron bombardment method, we used the 15 kV accelerating voltage. As seen in Figure 5 right, the spectral profiles of $M\alpha, \beta, \gamma$ diagram lines obtained in EPMA are very similar to those from the photon bombardment method with the double-crystal x-ray spectrometer. Moreover, a non-diagram line marked by D can be assigned by theoretical calculation as seen in Table 9. The spectrum abscissa was calibrated with respect to the line $M\gamma_1$ which is $M_3 - N_5$ as this is probably the binding energies we know best compared to other M lines.

4.2.1 The observed $M\alpha$, $M\beta$, and $M\gamma$ emission lines

The $M\alpha, \beta$ and $M\gamma$ diagram lines of gadolinium are presented in Fig. 5. In addition to these diagram lines, four peaks are resolved and labeled as A-D. These peaks are presented in Table 9 together with the results using EPMA. Bonnelle and Karnatak measured Gd $M\alpha$ and $M\beta$ in Gd metal and Gd_2O_3 compound [45]. They reported the effect of the compound, i.e. the chemical shift and the profile change. After then, LaVilla measured $M\alpha$ and $M\beta$ emission lines in Gd_2O_3 and Yb_2O_3 in order to investigate the resonance radiation using the fluorescence method using the double-crystal x-ray spectrometer [47], and indicated that Gd $M\alpha$ and $M\beta$ emission lines in Gd_2O_3 compound have a different aspect from those reported by Bonnelle and Kartanak.

Lines	Energy (eV)					FWHM (eV)		NIR
	Present		Cauchois [3]	Deslattes [5]			Campbell [72]	
	Exp.	Th.		Exp.	Th.	Exp.		
$L\beta_1$ ($L_2 - M_4$)	6713.42(13)	6711.29(20)	6713.21	6713.4(11)	6711.1(12)	6.45(6)	4.82	100
$L\beta_1$ hid. sat.	6708.17(23)					8.7(4)		19.8(23)
$L\beta_1$ vis. sat.	6737.49(25)		6741.05			9.47(21)		3.20(21)
$L\beta_4$ ($L_1 - M_2$)	6686.67(11)	6686.89(20)	6687.05	6687.3(11)	6684.8(23)	10.70(18)	9.40	14.08(19)
$L\beta_3$ ($L_1 - M_3$)	6831.50(16)	6832.16(20)	6831.12	6831.0(11)	6829.9(23)	13.82(12)	12.10	25.22(29)
$L\beta_6$ ($L_3 - N_1$)	6865.25(23)	6865.94(20)	6866.98	6867.3(11)	6863.8(36)	14.1(7)	8.62	2.58(18)
X ($L\beta_{14}$)	7075.77(17)		7075.91			10.41(31)		7.55(23)
$L\beta_{15}$ ($L_3 - N_4$)	7098.2(7)	7086.29(20)	7097.92	7103.0(12)	7093.9(26)	10.5(10)		5.1(26)
$L\beta_2$ ($L_3 - N_5$)	7102.38(18)	7102.91(20)	7103.05		7101.77(55)	6.90(19)	6.05	35.2(22)
$L\beta_{10}$ ($L_1 - M_4$)	7157.90(13)	7157.43(20)	7160.31	7160.4(18)	7155.0(20)	5.3(9)	4.75	0.33(9)
$L\beta_9$ ($L_1 - M_5$)	7190.75(12)	7191.88(20)	7191.74	7191.6(19)	7188.8(19)	9.8(11)	4.75	0.89(12)

Table 6: The averaged fitting parameters for the Gd $L\beta_{1,2,3,4,6,9,10,15}$ spectra using 11 symmetric Lorentzians to derive the contribution of the satellite and obtaining the natural linewidths. NIR stands for the normalized intensity ratio. The energy values are from Cauchois [3] and Deslattes *et al.* [5], respectively, and the FWHM are from Campbell and Papp [72]. Uncertainties are indicated within parentheses. The primary target was Rh and the spectrometer crystal was Ge(220) × 2.

Lines	Energy (eV)			FWHM (eV)		NIR
	Present	Cauchois	Deslattes [5]		Campbell	
	Exp.	[3]	Exp.	Exp.	[72]	
$L\beta_1$	6713.60(4)	6713.21	6713.4(11)	5.87(5)*	4.82	100
$L\beta_1$ hid. sat.	6708.29(11)			7.85(25)		18.1(11)
$L\beta_1$ vis. sat.	6737.47(6)	6741.05		7.7(4)		2.54(21)
$L\beta_4$	6687.06(6)	6687.05	6687.3(11)	10.32(9)	9.4	14.27(22)

Table 7: The averaged fitting parameters for the Gd $L\beta_{1,4}$ spectra using four symmetric Lorentzians to obtain the contribution of the satellite and the natural linewidths. NIR stands for the normalized intensity ratio, * is the CF, i.e. the corrected FWHM from the instrumental resolution. The energy values are from Cauchois [3] and Deslattes *et al.* [5], respectively, and the FWHM are from Campbell and Papp [72]. Uncertainties are indicated within parentheses.

4.2.2 Results and discussion

The features of lines named A and B observed in Figure 5 contain contributions from more than one transition. The feature named C was assigned to a $M\beta$ satellite. The diagram lines $M_5 - N_2$, $M\xi_1$ ($M_5 - N_3$), $M_4 - N_2$ and $M_4 - N_3$ have energies compatible with the binding energies M_5 and N_2 presented in Table 2 except for N_3 for which we found a difference of 20 eV. The $M\alpha_{2,1}$ ($M_5 - N_{6,7}$) at 1178.60 eV and $M\beta$ ($M_4 - N_6$) at 1209.84 eV gives $N_{6,7}$ = 11.5 eV and N_6 = 10.26 eV, which are compatible. These two peaks are surrounded by five other contributions. At energies 1160.2 and 1165.6 eV, we identify the $M_5 - O_2$ and $M_5 - O_3$ diagram lines, respectively. In this case, O_2 should take the value of 29.9 eV, and O_3, 24.5 eV. At 1188.5 and 1193.6 eV, we identify $M_4 - O_2$ and $M_4 - O_3$,respectively. This gives 31.6 and 16.5 eV for O_2 and O_3, respectively. Finally, the closed shells O_2 ($5p^{1/2}$) and O_3 ($5p^{3/2}$) are derived at 30.7 eV and 25.5 eV, respectively. Finally, the peak at 1541.1 eV is ascribed to the $M_3 - O_{4,5}$ because its level is very close from the binding energy.

Almost similar results are obtained with the photon bombardment experiment although the signal/background ratio is not as good as compared with that in EPMA. We performed the same considerations for $M\alpha_{2,1}$ ($M_5 - N_{6,7}$) at 1177.72 eV and $M\beta$ ($M_4 - N_6$) at 1208.97 eV, which gives $N_{6,7}$ = 12.4

Excitation method	$L_3 - M_{4,5}$		$M_{4,5} - N_{6,7}$		
	[76]	present	[47]	present	Diff.
photons (x-rays)	32.2	32.34	30.5	31.25	1.09
electrons (EPMA)				30.6	

Table 8: M4-M5 splitting (in eV).

Lines	Energy (eV)					Widths (eV)		NIR
	Present			Bearden	Cauchois	FWHM	FWHM	
	Exp. (Fluo)	Exp. (EPMA)	Th.	[76]	[3]	Exp. (Fluo)	Exp. (EPMA)	(Fluo)
$M_5 - N_2$		896.2(4)					16(3)	
$M\xi_1 (M_5 - N_3)$		915.14(3)	912.24(20)	914	913.74		8.9(2)	
$M_4 - N_2$		927.0(3)					9(2)	
$M_4 - N_3$		945.0(6)					17(3)	
A	1165.03(49)					11.1(9)		31.8(14)
$M_5 - O_2$		1160.2(10)					3(3)	
$M_5 - O_3$		1165.6(6)			1165.27		6.2(20)	
$M\alpha_{2,1}$ ($M_5 - N_{6,7}$)	1177.72(47)	1178.60(10)	1174.37(20)	1185	1180.47	5.06(52)	3.9(4)	47.2(13)
B	1193.0(5)				1187.03	11.9(8)		69.9(17)
$M_4 - O_2$		1188.5(5)					3.5(19)	
$M_4 - O_3$		1193.6(5)					8.2(13)	
$M\beta$ ($M_4 - N_6$)	1208.97(47)	1209.84(4)	1208.97(20)	1209.1	1209.97	4.53(37)	3.21(9)	100
$M\beta$ sat.	1221.3(5)	1222.0				11.4(10)	5.3(16)	29.6(16)
D	1379.6(4)	1381.7(18)	1385.99(20)			12.1(27)	10(4)	3.7(15)
$M\gamma_1$ ($M_3 - N_5$)	1403.1(5)	1404.4(2)	1402.68(20)	1402	1401.83	11.96(88)	13.3(5)	32.1(15)
$M_2 - N_4$			1531.63(20)					
$M_3 - O_{4,5}$		1544.1(5)			1541.17		13.5(15)	

Table 9: The averaged fitting parameters for gadolinium $M\alpha, \beta, \gamma$ spectra are shown for both the fluorescence and EPMA methods together with the theoretical calculations. NIR stands for the normalized intensity ratio. The energy value refers to Bearden [76] and Cauchois [3]. Uncertainties are indicated within parentheses. The primary target was Rh and the spectrometer crystal was TAP(001) × 2.

eV and N_6 = 11.1 eV. The N and O binding energies evaluated are averaged (when several values were derived) and gathered in Table 2 with other values from the literature for comparison.

The peaks of the $M\alpha$ and $M\beta$ emission lines obtained in fluorescence permits the measurement of the $M_4 - M_5$ spin-orbit splitting. The $M_4 - M_5$ splitting is ascertained also from the $L_3 - M_{4,5}$ emission lines in Table 8. The splitting derived from the $L_3 - M_{4,5}$ lines is larger by about 1.09 eV, which is similar to that reported by LaVilla [47]. He suggested that the difference is attributed to electrostatic interaction between the open $3d$ and $4f$ shells and when the $4f$ shell ($N_{6,7}$) is completed and lies deeper in the atoms as at higher Z number, the $M_4 - M_5$ splittings from the $L_3 - M_{4,5}$ and $M_{4,5} - N_6$ emission lines are equal within experimental uncertainties.

5 Conclusion

This work proposes a consistent set of binding energies and diagram lines energies for the L and M subshells of gadolinium by combining complementary x-ray techniques and a theoretical approach. We measured the mass attenuation coefficients of gadolinium in a large range from 100 eV to 25 keV using a well-established methodology, included reliable uncertainties. These values were used to derive the $L_{1,2,3}$, $M_{1,2,3,4,5}$ and $N_{1,2,3,4,5}$ binding energies that were used to check for consistency with the L lines

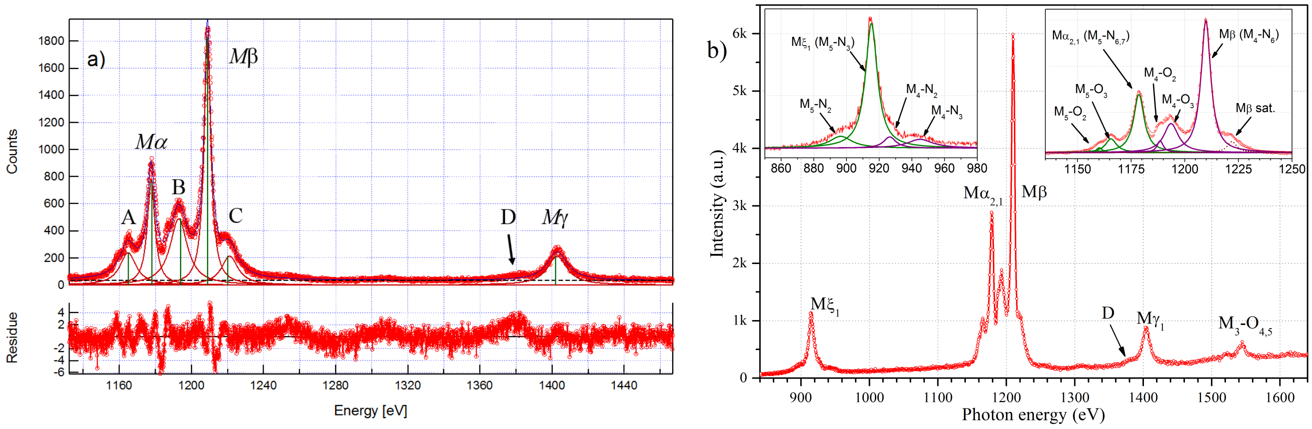

Figure 5: a) The observed $M\alpha, \beta, \gamma$ spectrum of Gd obtained with the antiparallel double-crystal x-ray spectrometer with TAP(001) crystals in photon bombardment. Several peaks marked by A, B. C, and D are shown together with Lorentzian functions used in the fitting process. b) The observed $M\alpha, \beta, \gamma, \xi$ spectra of Gd measured using EPMA method with analysing crystal TAP(001).

and to identify the M diagram lines. The gadolinium L and M spectral lines were measured accurately using the anti-parallel crystals x-ray spectrometer, and were compared with the most recent theoretical calculations that consider the electronic transitions. Moreover, the natural linewidths of $L\alpha_{1,2}$ and $L\beta_1$ diagram line were derived from the FWHMs obtained in the present study. The $L\beta_1$ hidden satellite, the $L\beta_{15}$ diagram line and a non-diagram line named $L\beta_{14}$ reported by Cauchois were confirmed. We report for the first time on the precise identification of the Gd M emission lines $M_5 - O_2$, $M_4 - O_{2,3}$ and $M_4 - N_{2,3}$ diagram lines.

6 Acknowledgments

Y. Ménesguen, M.-C. Lépy and Y. Ito acknowledge the financial support for the measurements of a part of the data by the REXDAB Collaboration that was initiated within the International Fundamental Parameter Initiative. This work was also supported by the National Science Centre, Poland under grant number 2017/25/B/ST2/00901 and by the research center grants UID/FIS/04559/2013 to LIBPhys-UNL, and UID/MULTI/04046/2013 to BioISI, from the FCT/MCTES/PIDDAC, Portugal. The Laboratoire Kastler Brossel is Unité Mixte de Recherche du CNRS, de l´ ENS et de l´UPMC No. 8552.

References

[1] C. Bonnelle and P. Motais, "$4f$-$3d$ emission spectra of the rare earths: An interpretation of the lines observed on both sides of the resonances," *Phys. Rev. A*, vol. 73, p. 042504, Apr 2006.

[2] F. B. Larkins, "Semiempirical Auger-electron energies for elements $10 \leq Z \leq 100$," *Atomic Data and Nuclear Data Tables*, vol. 20, pp. 311–387, 1977.

[3] Y. Cauchois and C. Sénémaud, *Wavelengths of x-ray emission lines and absorption edges*. Pergamon press, 1978.

[4] D. E. Cullen, J. H. Hubbell, and L. Kissel, "EPDL97: the Evaluated Photon Data Library, '97 Version"," *UCRL-50400*, vol. 6, no. 5, 1997, consultation date: 2017. [Online]. Available: https://www-nds.iaea.org/epdl97/document/epdl97.pdf

[5] R. D. Deslattes, E. G. Kessler, P. Indelicato, L. de Billy, E. Lindroth, and J. Anton, “X-ray transition energies: new approach to a comprehensive evaluation,” *Reviews of Modern Physics*, vol. 75, no. 1, pp. 35–99, 2003.

[6] Y. Ménesguen, C. Dulieu, and M.-C. Lépy, “Advances in the measurements of the mass attenuation coefficients,” *X-ray Spectrometry*, pp. 1–6, 2018.

[7] C. Bonnelle, R. C. Karnatak, and C. K. Jorgensen, “X-ray and photoelectron spectroscopy for the determination of 4f energies of rare earths,” *Chemical Physics Letters*, vol. 14, no. 2, pp. 145–149, 1972.

[8] M. Deutsch, G. Hölzer, J. Härtwig, J. Wolf, M. Fritsch, and E. Förster, “$K\alpha$ and $K\beta$ x-ray emission spectra of copper,” *Physical Review A*, vol. 51, p. 283, 1995.

[9] G. Hölzer, M. Fritsch, M. Deutsch, J. Härtwig, and E. Förster, “$K\alpha_{1,2}$ and $K\beta_{1,3}$ x-ray emission lines of the 3d transition metals,” *Phys. Rev. A*, vol. 56, pp. 4554–4568, Dec 1997.

[10] S. Porikli, “Influence of the chemical environment changes on the line shape and intensity ratio values for La, Ce and Pr L lines spectra,” *Chemical Physics Letters*, vol. 508, pp. 165–170, 2011.

[11] J. Finster, G. Leonhardt, and A. Meisel, “On the shape and the width of the main lines of x-ray emission of the 3d and 4d elements,” *Journal de Physique des Colloques*, vol. 32, pp. C4–218, 1971.

[12] B. Ekstig, E. Källne, E. Noreland, and R. Manne, “Electron interaction in x-ray emission spectra,” *Journal de Physique des Colloques*, vol. 32, pp. C4–214, 1971.

[13] M. Pessa, E.-K. Kortela, A. Suikkanen, and E. Suoninen, “Fine Structure of the Ti $k\beta_1\beta^{'}$ X-Ray Emission Spectrum,” *Phys. Rev. A*, vol. 8, pp. 48–50, Jul 1973.

[14] M. Deutsch, O. Gang, G. Hölzer, J. Härtwig, J. Wolf, M. Fritsch, and E. Förster, “$l_{2,3}$ and $m_{2,3}$ level widths and fluorescence yields of copper,” *Phys. Rev. A*, vol. 52, pp. 3661–3668, Nov 1995.

[15] M. J. Druyvesteyn, “Das Röntgenspektrum zweiter Art,” *Zeischrift für Physik*, vol. 43, pp. 707–725, 1927.

[16] S. Doniach and M. Sunjic, “Many-electron singularity in X-ray photoemission and X-ray line spectra from metals,” *Journal of Physics C: Solid State Physics*, vol. 3, p. 285, 1970.

[17] K. Tsutsumi, “The X-ray Non-diagram Lines $K\beta'$ of Some Compounds of the Iron Group,” *Journal of the Physical Society of Japan*, vol. 14, pp. 1696–1706, 1959.

[18] A. Faessler and G. Wiech, Eds., *X-ray spectra and electronic structure of matter: proceedings of the international symposium, München, September 1972*, vol. 1. München: Fotodruck Frank OHG, 1973.

[19] K. Tsutsumi, Y. Iwasaki, O. Aita, K. Ichikawa, and T. Watanabe, “X-Ray Spectroscopic Study of Valence Band of Transition-Metal Compounds,” *Journal of the Physical Society of Japan*, vol. 47, pp. 1920–1926, 1979.

[20] S. I. Salem, G. M. Hockney, and P. L. Lee, “Splitting of the $3p$ levels in the transition elements and their oxides,” *Phys. Rev. A*, vol. 13, pp. 330–334, Jan 1976.

[21] K. S. Srivastava, R. L. Shrivastava, O. K. Harsh, and V. Kumar, “Low-energy plasmon $k\beta^{'}$ satellite in the $k\beta_{1,3}$ x-ray emission spectra of mn, cr, and their compounds,” *Phys. Rev. B*, vol. 19, pp. 4336–4339, Apr 1979.

[22] K. S. Srivastava, S. Singh, A. K. Srivastava, R. S. Nayal, A. Chaubey, and P. Gupta, "Electron-electron interaction in transition-metal x-ray emission spectra," *Phys. Rev. A*, vol. 25, pp. 2838–2844, May 1982.

[23] D. F. Anagnostopoulos, R. Sharon, D. Gotta, and M. Deutsch, "$K\alpha$ and $K\beta$ x-ray emission spectra of metallic scandium," *Physical Review A*, vol. 60, p. 2018, 1999.

[24] C. T. Chantler, M. N. Kinnane, C.-H. Su, and J. A. Kimpton, "Characterization of $K\alpha$ spectral profiles for vanadium, component redetermination for scandium, titanium, chromium, and manganese, and development of satellite structure for Z=21 to Z=25," *Physical Review A*, vol. 73, p. 012508, 2006.

[25] Y. Ito, T. Tochio, and A. M. Oohashi, H.and Vlaicu, "Contribution of the [1s3d] shake process to $K\alpha_{1,2}$ spectra in 3d elements," *Radiation Physics and Chemistry*, vol. 75, p. 1534, 2006.

[26] Y. Ito, T. Tochio, H. Ohashi, M. Yamashita, S. Fukushima, M. Polasik, K. Słabkowska, . Syrocki, E. Szymańska, J. Rzadkiewicz, P. Indelicato, J. P. Marques, M. C. Martins, J. P. Santos, and F. Parente, "$K\alpha_{1,2}$ x-ray linewidths, asymmetry indices, and [KM] shake probabilities in elements Ca to Ge and comparison with theory for Ca, Ti, and Ge," *Physical Review A*, vol. 94, p. 042506, 2016.

[27] T. Ishizuka, *Advances in X-ray Chemical Analysis*, vol. 30, p. 21, 1998.

[28] T. L. Pham, T. V. Nguyen, J. A. Lowe, I. P. Grant, and C. T. Chantler, "Characterization of the copper $K\beta$ x-ray emission profile: an ab initio multi-configuration Dirac–Hartree–Fock approach with Bayesian constraints," *Journal of Physics B: Atomic, Molecular and Optical Physics*, vol. 49, no. 3, p. 035601, jan 2016.

[29] W. C. Sauder, J. R. Huddle, J. D. Wilson, and R. E. Lavilla, "Detection of multiple structure in cu $K\alpha_{1,2}$ by means of a monolithic double crystal spectrometer," *Physics Letters A*, vol. 63, no. 3, pp. 313–315, 1977.

[30] R. E. LaVilla, "Double-vacancy transitions in the copper $K\beta_{1,3}$ emission spectrum," *Phys. Rev. A*, vol. 19, pp. 717–720, Feb 1979.

[31] J. Bremer and H. Sorum, "A highly resolved Cu $K\beta_{1,3}$-intensity distribution," *Physics Letters A*, vol. 75, pp. 47–49, 1979.

[32] R. D. Deslattes, R. E. Lavilla, and A. Henins, "Double monochromator systems for the study of multiple vacancy processes," *Nuclear Instruments & Methods*, vol. 152, pp. 179–183, June 1978.

[33] Y. Ito, T. Tochio, M. Yamashita, S. Fukushima, A. M. Vlaicu, L. Syrocki, K. Słabkowska, E. Weder, M. Polasik, K. Sawicka, P. Indelicato, J. P. Marques, J. M. Sampaio, M. Guerra, J. P. Santos, and F. Parente, "Structure of high-resolution $K\beta_{1,3}$ x-ray emission spectra for the elements from Ca to Ge," *Physical Review A*, vol. 97, no. 5, p. 052505, May 2018.

[34] S. P. Durdaği, "Chemical environment change analysis on L X-ray emission spectra of some lanthanide compounds," *Microchemical Journal*, vol. 130, pp. 27 – 32, 2017.

[35] C. V. Raghavaiah, N. Venkateswara Rao, S. Bhuloka Reddy, G. Satyanarayana, and D. L. Sastry, "$L\alpha/L_l$ X-ray intensity ratios for elements in the region 55 $\leq$Z$\leq$ 80," *Journal of Physics B: Atomic and Molecular Physics*, vol. 20, no. 21, pp. 5647–5651, nov 1987.

[36] S. Durdaği, "Effect of applied external magnetic field on the L X-ray emission line structures of the lanthanide elements," *Radiation Physics and Chemistry*, vol. 92, pp. 1 – 7, 2013.

[37] P. A. Cox, Y. Bear, and C. K. Jorgensen, *Chemical Physics Letters*, vol. 22, pp. 433–438, 1973.

[38] N. Spector, C. Bonnelle, C. Dufour, C. K. Jorgensen, and H. Berthou, *Chemical Physics Letters*, vol. 41, pp. 199–204, 1976.

[39] Y. Baer, R. Hauger, C. Zurcher, M. Campagna, and G. K. Wertheim, *Phys. Rev. B*, vol. 15, pp. 4433–4439, 1978.

[40] S. Tanaka, H. Ogasawara, K. Okada, and A. Kotani, *Journal of Electron Spectroscopy and Related Phenomena*, vol. 79, pp. 199–202, 1996.

[41] T. Jo and A. Tanaka, *Journal of the Physical Society of Japan*, vol. 67, pp. 1457–1465, 1998.

[42] D. L. Ederer, A. Moewes, E. Z. Kurmaev, T. A. Callcott, M. M. Grush, S. Stadler, R. Winarski, R. C. C. Perera, and L. J. Terminello, *Journal of Physics and Chemistry of Solids*, vol. 61, pp. 435–444, 2000.

[43] A. R. H. Preston, B. J. Ruck, W. R. L. Lambrecht, L. F. J. Piper, J. E. Downes, K. E. Smith, and H. J. Trodahl, *Applied Physics Letters*, vol. 96, p. 032101, 2010.

[44] J. G. Tobin, S. W. Yu, B. W. Chung, G. D. Waddill, L. Duda, and J. Nordgren, *Phys. Rev. B*, vol. 83, p. 085104, 2011.

[45] C. Bonnelle and R. C. Karnatak, “Spectres M du gadolinium dans le métal et l’oxyde,” *Comptes rendus de l’académie des Sciences*, vol. 268, pp. 494–497, 1969.

[46] ——, “Distributions des états f dans les métaux et les oxydes de terres rares,” *Journal de Physique Colloques*, vol. 32, pp. C4–230, 1971.

[47] R. E. LaVilla, “$M_{4,5}$ emission spectra from Gd_2O_3 and Yb_2O_3,” *Phys. Rev. A*, vol. 9, pp. 1801–1805, May 1974.

[48] Y. Ménesguen, M. Gerlach, B. Pollakowski, R. Unterumsberger, M. Haschke, B. Beckhoff, and M.-C. Lépy, “High accuracy experimental determination of copper and zinc mass attenuation coefficients in the 100 eV to 30 keV photon energy range,” *Metrologia*, vol. 53, pp. 7–17, 2016.

[49] Y. Ménesguen, M.-C. Lépy, P. Hönicke, M. Müller, R. Unterumsberger, B. Beckhoff, J. Hoszowska, J.-Cl. Dousse, W. Błachucki, Y. Ito, M. Yamashita, and S. Fukushima, “Experimental determination of the x-ray atomic fundamental parameters of nickel,” *Metrologia*, vol. 55, pp. 56–66, 2018.

[50] Y. Ménesguen, M.-C. Lépy, J. M. Sampaio, J. P. Marques, F. Parente, M. Guerra, P. Indelicato, J. P. Santos, P. Hönicke, and B. Beckhoff, “A combined experimental and theoretical approach to determine X-ray atomic fundamental quantities of tin,” *X-Ray Spectrometry*, pp. 1–11, 2018.

[51] Y. Ménesguen and M.-C. Lépy, “Mass attenuation coefficients in the range $3.8 \leq E \leq 11$ kev, K fluorescence yield and K_β/K_α relative X-ray emission rate for Ti, V, Fe, Co, Ni, Cu, and Zn measured with a tunable monochromatic X-ray source,” *Nuclear Instruments & Methods In Physics Research B*, vol. 268, no. 16, pp. 2477–2486, 2010.

[52] Goodfellow Cambridge Limited (GB). Consultation date: 2015. [Online]. Available: http://www.goodfellow.com/

[53] JCGM, *Evaluation of measurement data - Guide to the expression of uncertainty in measurement.* BIPM, 2008, consultation date: 2015. [Online]. Available: http://www.bipm.org/fr/publications/guides/gum.html

[54] B. L. Henke, E. M. Gullikson, and J. C. Davis, “X-ray interactions: photoabsorption, scattering, transmission, and reflection at E = 50-30000 eV, Z = 1-92,” *Atomic Data and Nuclear Data Tables*, vol. 54, no. 2, pp. 181–342, 1993.

[55] C. T. Chantler, "Theoretical form factor, attenuation and scattering tabulations for Z=1-92 from E=1-10 eV to E=0.4-1.0 MeV," *Journal of Physical and Chemical Reference Data*, vol. 24, pp. 71–643, 1995.

[56] M. J. Berger, J. H. Hubbell, S. M. Seltzer, J. Chang, J. S. Coursey, R. Sukumar, and D. S. Zucker, *XCOM: Photon Cross Section Database (version 3.1)*, National Institute of Standards and Technology Std., 2010, consultation date: 2017. [Online]. Available: https://www.nist.gov/pml/xcom-photon-cross-sections-database

[57] M. O. Krause, C. W. Nestor, C. J. Sparks, and E. Ricci, "X-ray fluorescence cross sections for K and L X-rays of the elements," *Oak Ridge National Laboratory*, vol. 5399, 1978.

[58] I. P. Grant, "Relativistic atomic structure theory: Some recent work," *International Journal of Quantum Chemistry*, vol. 25, no. 23, pp. 23–46, 1984.

[59] K. G. Dyall, I. P. Grant, C. T. Johnson, F. A. Parpia, and E. P. Plummer, "GRASP: A general-purpose relativistic atomic structure program," *Computer Physics Communications*, vol. 55, no. 3, pp. 425–456, 1989.

[60] M. Polasik, "Theoretical multiconfiguration Dirac-Fock method study on the x-ray spectra of multiply ionized heavy atoms: The structure of the $K\alpha\ L^n$ lines," *Physical Review A*, vol. 39, p. 616, 1989.

[61] ——, "Theoretical simulation of the x-ray spectra of multiply ionized heavy atoms: The $K\alpha\ L^n$ spectra of molybdenum," *Physical Review A*, vol. 39, p. 5092, 1989.

[62] ——, "Theoretical multiconfiguration Dirac-Fock method study on the x-ray spectra of multiply ionized heavy atoms: The structure of the $K\alpha L^0 M^r$ lines," *Phys. Rev. A*, vol. 40, pp. 4361–4368, Oct 1989.

[63] ——, "Theoretical multiconfiguration Dirac-Fock method study on the x-ray spectra of multiply ionized heavy atoms: The structure of the $K\alpha L^1 M^r$ satellite lines," *Phys. Rev. A*, vol. 41, pp. 3689–3697, Apr 1990.

[64] ——, "Systematic multiconfiguration-Dirac-Fock study of the x-ray spectra accompanying the ionization in collision processes: The structure of the $K\beta_{1,3}L^0M^r$ lines," *Phys. Rev. A*, vol. 52, pp. 227–235, Jul 1995.

[65] ——, "Influence of changes in the valence electronic configuration on the $K\beta$-to-$K\alpha$ x-ray intensity ratios of the 3d transition metals," *Physical Review A*, vol. 58, no. 3, pp. 1840–1845, Sep 1998.

[66] F. A. Parpia, C. Froese Fischer, and I. P. Grant, "GRASP92: A package for large-scale relativistic atomic structure calculations," *Computer Physics Communications*, vol. 94, pp. 249–271, 1996.

[67] P. Jönsson, X. He, C. Froese Fischer, and I. P. Grant, "The grasp2K relativistic atomic structure package," *Computer Physics Communications*, vol. 177, no. 7, pp. 597–622, 2007.

[68] M. Polasik, K. Słabkowska, J. Rzadkiewicz, K. Kozioł, J. Starosta, E. Wiatrowska-Kozioł, J.-Cl. Dousse, and J. Hoszowska, "$K^h\alpha_{1,2}$ X-Ray Hypersatellite Line Broadening as a Signature of K-Shell Double Photoionization Followed by Outer-Shell Ionization and Excitation," *Phys. Rev. Lett.*, vol. 107, p. 073001, Aug 2011.

[69] J. P. Desclaux, "A multiconfiguration relativistic Dirac-Fock program," *Computer Physics Communications*, vol. 9, no. 1, pp. 31–45, 1975.

[70] P. Indelicato, "Projection operators in multiconfiguration Dirac-Fock calculations: Application to the ground state of heliumlike ions," *Physical Review A*, vol. 51, p. 1132, 1995.

[71] T. Tochio, Y. Ito, and K. Omote, “Broadening of the x-ray emission line due to the instrumental function of the double-crystal spectrometer,” *Physical Review A*, vol. 65, p. 042502, 2002.

[72] J. L. Campbell and T. Papp, “Widths of atomic K-N7 levels,” *Atomic Data and Nuclear Data Tables*, vol. 77, pp. 1–56, 2001.

[73] H. Berger, “Study of the $K\alpha$ emission spectrum of copper,” *X-ray spectrometry*, vol. 15, no. 4, pp. 241–243, 1986.

[74] M. H. Krisch, F. Sette, U. Bergmann, C. Masciovecchio, R. Verbeni, J. Goulon, W. Caliebe, and C. C. Kao, “Observation of magnetic circular dichroism in resonant inelastic x-ray scattering at the L_3 edge of gadolinium metal,” *Physical Review B*, vol. 54, p. R12673, 1996.

[75] M. H. Krisch, F. Sette, C. Masciovecchio, and R. Verbeni, “X-ray resonant Raman scattering from $Gd_3Fe_5O_{12}$,” *Journal of Electron Spectroscopy and Related Phenomena*, vol. 86, pp. 159–164, 1997.

[76] J. A. Bearden, “X-Ray Wavelengths,” *Review of Modern Physics*, vol. 39, p. 78, 1967.

[77] P. Sakellaridis, “Multiplets caractéristiques des terres rares dans leurs spectres d’émission X,” *Journal de Physique*, vol. 16, pp. 422–427, 1955.